Geometrical protection of topological magnetic solitons in microprocessed chiral magnets

doi: https://doi.org/10.1103/PhysRevB.97.024408

Geometrical protection of topological magnetic solitons in microprocessed chiral magnets

Masaki Mito,[1,2,*] Hiroyuki Ohsumi,[3] Kazuki Tsuruta,[4] Yoshinori Kotani,[4] Tetsuya Nakamura,[4] Yoshihiko Togawa,[2,5] Misako Shinozaki,[6] Yusuke Kato,[6,7] Jun-ichiro Kishine,[2,8] Jun-ichiro Ohe,[9] Yusuke Kousaka,[2,10] Jun Akimitsu,[10] and Katsuya Inoue[2,11,12]

[1]*Faculty of Engineering, Kyushu Institute of Technology, Kitakyushu 804-8550, Japan*
[2]*Chirality Research Center, Hiroshima University, Higashihiroshima 739-8526, Japan*
[3]*RIKEN SPring-8 Center, Hyogo 679-5148, Japan*
[4]*Japan Synchrotron Radiation Research Institute, Hyogo 679-5198, Japan*
[5]*Department of Physics and Electronics, Osaka Prefecture University, Sakai 599-8570, Japan*
[6]*Department of Basic Science, The University of Tokyo, Tokyo 153-8902, Japan*
[7]*Department of Physics, The University of Tokyo, Tokyo 113-0033, Japan*
[8]*Graduate School of Arts and Sciences, The Open University of Japan, Chiba 261-8586, Japan*
[9]*Department of Physics, Toho University, Chiba 274-8510, Japan*
[10]*Research Institute for Interdisciplinary Science, Okayama University, Okayama 700-8530, Japan*
[11]*Graduate School of Science, Hiroshima University, Higashihiroshima 739-8526, Japan*
[12]*Institute for Advanced Materials Research, Hiroshima University, Higashihiroshima 739-8526, Japan*

(Received 25 September 2017; published 9 January 2018)

A chiral soliton lattice stabilized in a monoaxial chiral magnet $CrNb_3S_6$ is a magnetic superlattice consisting of magnetic kinks with a ferromagnetic background. The magnetic kinks are considered to be topological magnetic solitons (TMSs). Changes in the TMS number yield discretized responses in magnetization and electrical conductivity, and this effect is more prominent in smaller crystals. We demonstrate that, in microprocessed $CrNb_3S_6$ crystals, TMSs are geometrically protected through element-selected micromagnetometry using soft x-ray magnetic circular dichroism (MCD). A series of x-ray MCD data is supported by mean-field and micromagnetic analyses. By designing the microcrystal geometry, TMS numbers can be successfully changed and fixed over a wide range of magnetic fields.

DOI: 10.1103/PhysRevB.97.024408

I. INTRODUCTION

A violation of space-inversion symmetry entails a Dzyaloshinskii-Moriya (D-M) interaction originating from the spin-orbit interaction [1,2], which stabilizes a chiral helimagnetic spin alignment [Fig. 1(a)]. It provides a promising scientific field for topological magnetic solitons (TMSs) [3]. The chiral helimagnetic texture is not equivalent to the helimagnetic texture stabilized in rare-earth metals, where conduction electrons mediate interaction between 4f localized moments. In the latter, two types of helicities coexist.

For instance, in monoaxial chiral magnets with a type of D-M vector, a dc magnetic field H perpendicular to the chiral helical axis untwists the helimagnetic alignment toward the forced-ferromagnetic state [Fig. 1(c)] via the formation of a chiral soliton lattice [CSL; Fig. 1(b)] [4–6]. Here, the magnetic kink type of solitonic object is a TMS. The intermediate CSL is a spin superlattice that consists of 2π-twisted TMSs partitioned by ferromagnetic parts. On the other hand, in the cubic chiral magnets with three equivalent D-M vectors such as MnSi [7,8] and FeGe [9], the vortex type of solitonic object constructs the two-dimensional solitonic texture termed the skyrmion lattice in the finite H region [10,11]. The skyrmion lattice is influenced by the geometry of the specimens [12–14]. Thus, in experimental studies of TMSs, the technique of microfabrication is important.

In a prototype monoaxial chiral magnet, $CrNb_3S_6$, Lorentz TEM observations on microprocessed specimens proved the existence of CSL [6,15]. Changes in the TMS number were detected via incremental changes in magnetoresistance [6,16], indicating that the TMS number behaves as a topological quantum number [16,17]. Early studies on bulk $CrNb_3S_6$ crystals showed a near-reversible magnetization [18,19], which was reproduced by mean-field (MF) results determined by the minimum-energy conditions [4,5]. However, on reducing the total number of TMSs that the soliton system holds, the topological nature of the TMSs manifests as a discretized response of physical properties such as magnetoresistance, magnetic torque, and magnetic resonance [6,16,20–22]. Indeed, as suggested theoretically in a few TMS systems [23], precise magnetization measurements with minute H steps showed several tiny magnetization jumps, even in millimeter-sized single crystals [18,24,25].

Thus, specimens with dimensions reduced down to less than the crystalline grain size are advantageous to demonstrate the existence of the chiral solitons and their size effects [6,16]. A magnetoresistance measurement of a micrometer-scale specimen demonstrated the soliton confinement effects in a finite-size system [16], yielding important evidence of topological

*mitoh@mns.kyutech.ac.jp

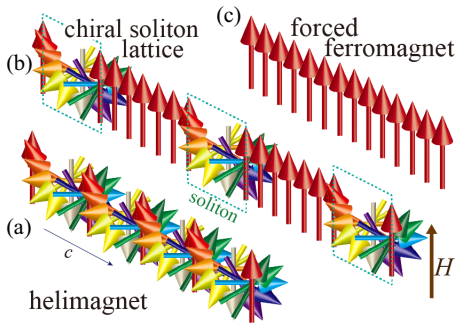

FIG. 1. Images of (a) a helimagnet, (b) a chiral soliton lattice, and (c) a forced ferromagnet. In (b), the dc magnetic field H applied to the chiral helical axis stabilizes CSL.

spin texture triggered by the D-M interaction. Here, further accumulation of magnetic data on the finite-size effects should lead to a deeper understanding of chiral solitons. Although technical difficulties impede highly sensitive magnetometry in microprocessed specimens, revealing the fundamental process by which TMSs are inserted or released in the system and identifying a method of controlling and manipulating the number of TMSs remain important areas of research. We address these questions by measuring the element-specific magnetization for Cr ions M_{Cr} using soft x-ray magnetic circular dichroism (MCD) in microprocessed specimens and by comparing the experimental results with numerical calculations.

II. METHODS

A. Materials

A single crystal of $CrNb_3S_6$ was synthesized using a previously described procedure [26]. Micrometer-scale crystals that were typically $10 \times 10 \times 1$ μm^3 in size were cut from the single crystal using a focused ion beam, and the thickness of the area exposed to measurement was reduced to approximately 0.1 μm. Specimens A, B, and C were mounted over a 5-μm-diameter pinhole in a Ta plate (Fig. S1 [27]) by locally depositing tungsten, as shown in Figs. 2(a)–2(c). The Ta plate is impermeable to x rays, and therefore, the magnetic data were detected from only the central part of the specimen that was located over the pinhole. For specimen C, the surrounding wall with a height of 1 μm was removed after the thinning and mounting processes.

B. X-ray magnetic circular dichroism

The soft x-ray MCD measurement of a transmission mode was conducted using the twin-helical undulator beamline, BL25SU, of SPring-8 [28]. The microprocessed specimen on the Ta substrate was fixed to the top of a cryotube with an indium thermal conductive sheet. The thickness of the specimen's transparent area, namely, the transmission length for the MCD measurement, was approximately 0.10 μm. The measurements in transmittance mode were performed at 10 and 36 K, which are sufficiently lower than the critical temperature of approximately 130 K. The angle between the direction of the magnetic field H and the x-ray beam axis was fixed to be 10°. The x-ray beam axis was tuned to be perpendicular

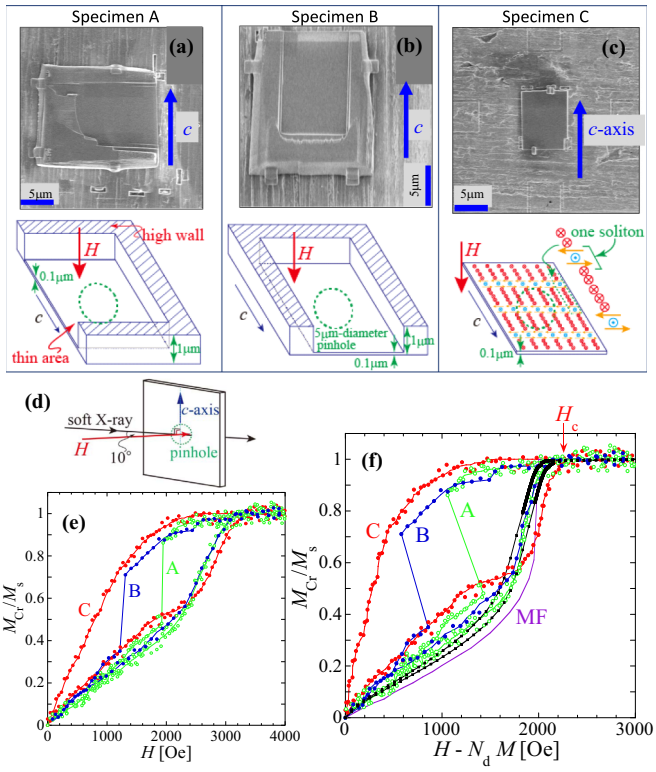

FIG. 2. Images and schematics of micrometer-sized $CrNb_3S_6$ specimens (a) A, (b) B, and (c) C, each attached to a Ta plate pierced by a single 5-μm-diameter pinhole (green dotted circle). (d) Overview of the experimental setup of soft x-ray MCD measurement. Both the x-ray beam axis and magnetic field H were perpendicular to the chiral helical axis (c axis; see the text). (e) Hysteresis curves of element-specific magnetization for Cr M_{Cr} obtained by the soft x-ray MCD measurements at $T = 10$ K. The MCD signal was observed over only the areas marked with green dots in (a)–(c). (f) Hysteresis curves of M_{Cr} after calibrating the demagnetization effect. The black solid squares and purple curve represent bulk millimeter-sized crystals from [24] and the mean-field (MF) theoretical results tracing the minimum-energy state for an infinite system, respectively [5]. In both (e) and (f), M_{Cr} is normalized to the saturated magnetization M_s.

to the sample surface in order to thread the beam into the channel with a diameter of 5 μm, fabricated in the Ta substrate. Indeed, as Fig. 2(d) shows, H was applied perpendicular to the chiral helical axis (c axis). The energy of the x ray was fixed at 576 eV, corresponding to L_3 of Cr (see Fig. S2 [27]), to obtain the element-specific magnetization for Cr M_{Cr}. The demagnetization effect was calibrated as $H_{\mathrm{eff}} = H - N_{\mathrm{d}} M_{\mathrm{Cr}}$, where M_{Cr} was evaluated in units of emu/cm^3 based on the volume of the measured region in the MCD experiment and previous results for a bulk single crystal [24,25]. In the present transmittance mode measurement for specimens A, B, and C, the specimen space exposed to measurement can be considered to be a thin disk with a diameter of 5 μm and thickness of 0.1 μm. Thus, the demagnetization field coefficient N_{d} was determined to be 1 for the very thin case in which H was applied approximately perpendicular to the sample surface. In the analysis, the same N_{d} was used for three specimens. For reference, we have to consider another N_{d} for the wall surrounding the measured part. The MCD signal was recorded

using the helicity switching method at a frequency of 1 Hz. M_{Cr} was measured by observing the averaged absorption intensities between the positive and negative helicities. The incident and transmitted x-ray beam intensities were recorded following a total electron yield method and p-i-n type (PIN) photodiode detection, respectively.

C. Three-dimensional mean-field theory

We analyzed a spin model for a monoaxial chiral helimagnet on a three-dimensional (3D) cubic lattice using a MF method [29]. Considering the cubic lattice as a set of layers, we labeled each site on the cubic lattice by a dimensionless vector $i = i_{||}\hat{\boldsymbol{z}} + \boldsymbol{i}_{\perp}$, with the integer $i_{||}$ specifying a layer and the two-dimensional vector $\boldsymbol{i}_{\perp} = i_x\hat{\boldsymbol{x}} + i_y\hat{\boldsymbol{y}}$ with integers i_x and i_y specifying a site in the layer. Here, $\hat{\boldsymbol{x}}$, $\hat{\boldsymbol{y}}$, and $\hat{\boldsymbol{z}}$ denote the unit vectors in the x, y, and z directions, respectively. The Hamiltonian is given by

$$\mathscr{H} = -J^{\perp}\sum_{\boldsymbol{i}}\boldsymbol{S}_i\cdot(\boldsymbol{S}_{i+\hat{\boldsymbol{x}}} + \boldsymbol{S}_{i+\hat{\boldsymbol{y}}}) - J^{||}\sum_{\boldsymbol{i}}\boldsymbol{S}_{\boldsymbol{i}}\cdot\boldsymbol{S}_{i+\hat{\boldsymbol{z}}} - D\sum_{\boldsymbol{i}}(\boldsymbol{S}_{\boldsymbol{i}}\times\boldsymbol{S}_{i+\hat{\boldsymbol{z}}})\cdot\hat{\boldsymbol{z}} - H\sum_{\boldsymbol{i}}\boldsymbol{S}_{\boldsymbol{i}}\cdot\hat{\boldsymbol{x}}, \quad (1)$$

where $\boldsymbol{S}_{\boldsymbol{i}}$ denotes a classical Heisenberg spin with the magnitude $S = 3/2$ at site i. The magnitudes of the D-M interaction vector D and the ferromagnetic exchange interactions $J^{||}$ and $J^{\perp}$ are considered only for the nearest-neighboring spins. We applied the external field (with strength H) perpendicular to the chiral helical axis. We set $J^{\perp}/J^{||} = 8$ and $D/J^{||} = 0.16$ to model $CrNb_3S_6$, and we set the number of layers $N_z = 4125$, which corresponds to 5 μm in this material. In the MF approximation, the system is mapped onto a single-spin model expressed as

$$\mathscr{H} = -\sum_{\boldsymbol{i}}\boldsymbol{H}^{\mathrm{mf}}_{i_{||}}\cdot\boldsymbol{S}_{\boldsymbol{i}} + \sum_{\boldsymbol{i}}C_{i_{||}}, \quad (2)$$

with the effective field in the $i_{||}$th layer

$$\boldsymbol{H}^{\mathrm{mf}}_{i_{||}} = 4J^{\perp}\boldsymbol{M}_{i_{||}} + J^{||}\left(\boldsymbol{M}_{i_{||}+1} + \boldsymbol{M}_{i_{||}-1}\right) + D\left(\boldsymbol{M}_{i_{||}+1} - \boldsymbol{M}_{i_{||}-1}\right)\times\hat{\boldsymbol{z}} + H\hat{\boldsymbol{x}} \quad (3)$$

and the constant term $C_{i_{||}} = (\boldsymbol{H}^{\mathrm{mf}}_{i_{||}} - H\hat{\boldsymbol{x}})\cdot\boldsymbol{M}_{i_{||}}/2$. Here,

$$\boldsymbol{M}_{i_{||}} = \langle\boldsymbol{S}_{\boldsymbol{i}}\rangle = \left[S\coth\left(\beta S\boldsymbol{H}^{\mathrm{mf}}_{i_{||}}\right) - \frac{1}{\beta\boldsymbol{H}^{\mathrm{mf}}_{i_{||}}}\right]\frac{\boldsymbol{H}^{\mathrm{mf}}_{i_{||}}}{|\boldsymbol{H}^{\mathrm{mf}}_{i_{||}}|}, \quad (4)$$

with $\beta = 1/k_{\mathrm{B}}T$ represents the thermal average of the spin moment in the $i_{||}$th layer. We assumed that $C_{i_{||}}$, $\boldsymbol{H}^{\mathrm{mf}}_{i_{||}}$, and $\boldsymbol{M}_{i_{||}}$ are independent of the index $\boldsymbol{i}_{\perp}$, and we solved these MF equations self-consistently using the following algorithm: (i) For a set of parameters ($J^{||}$, $J^{\perp}$, D, H, T), prepare initial conditions in the form $\boldsymbol{M}_{i_{||}} = S(\cos ki_{||}, \sin ki_{||}, 0)$, with $k = 2\pi w/N_z$ for the soliton number $w = 0,1,2,\ldots,105$. (ii) Calculate $\boldsymbol{H}^{\mathrm{mf}}_{i_{||}}$ and $\boldsymbol{M}_{i_{||}}$ for the $i_{||}$th layer for each initial state characterized by a soliton number w. In this work, we impose a periodic boundary condition. (iii) Perform the second step for all layers. Steps (ii) and (iii) constitute one iteration. (iv) Perform 10^7 iterations. We then obtain a spin configuration for a given set of parameters ($J^{||}$, $J^{\perp}$, D, H, T) for each initial state, and the physical properties such as the magnetization $\boldsymbol{M}/S = \Sigma_{i_{||}}\boldsymbol{M}_{i_{||}}/(N_zS)$ can be calculated using this configuration for each w. Because of the periodic boundary condition, w is conserved in steps (ii) through (iv). (v) Change H with the other parameters fixed, and perform steps (ii) through (iv) again. After performing this step for several values of H, we obtain the magnetization curves for a constant w.

D. Micromagnetic simulation

We performed a micromagnetic simulation that integrates the time evolution of the Landau-Lifshitz-Gilbert equation,

$$\frac{\partial\boldsymbol{S}}{\partial t} = -\gamma\boldsymbol{S}\times\boldsymbol{H}_{\mathrm{eff}} + \alpha\left(\boldsymbol{S}\times\frac{\partial\boldsymbol{S}}{\partial t}\right), \quad (5)$$

where $\boldsymbol{S}$ is the local spin, γ is the gyromagnetic ratio, and α is the Gilbert damping coefficient. $\boldsymbol{H}_{\mathrm{eff}}$ is the effective magnetic field obtained by $\boldsymbol{H}_{\mathrm{eff}} = -\frac{\partial E}{\partial\boldsymbol{S}}$, where E is the total energy of the spin system including the ferromagnetic exchange coupling and the D-M interaction D. We apply the fourth-order Runge-Kutta method to calculate the time evolution of the Landau-Lifshitz-Gilbert equation using a two-dimensional square lattice with the lattice constant $a = 1$ nm. Magnetization curves were calculated for a system landscape containing 500 × 20 unit cells. The magnetic field H was applied perpendicular to the square lattice. The exchange energy along the c axis $J^{||}$ was 29 K, and that in the in-plane direction $J^{\perp}$ was 232 K: The energy of D was 3 K. We assume that the unit cell (1 nm^3) includes $3\mu_{\mathrm{B}}$. To obtain the ground state, we prepared a random state and performed the time evolution of the Landau-Lifshitz-Gilbert equation with a large damping coefficient ($\alpha = 0.1$). We introduce the finite-temperature effect by applying a random magnetic field $\boldsymbol{h}$ in which the variance proportional to the temperature is as follows: $\langle h_\mu(t)h_\nu(t')\rangle = \frac{2\alpha k_{\mathrm{B}}T}{VM_{\mathrm{S}}\gamma}\delta_{\mu\nu}\delta(t-t')$, where α is the Gilbert damping, V is the volume of the unit cell in the simulation, M_{S} is the saturation magnetization, and γ is the gyromagnetic ratio [30]. The magnetization curve was obtained by varying H (at a ratio of 10 Oe/ns).

III. RESULTS

A. X-ray magnetic circular dichroism

Figures 2(a)–2(c) present microprocessed $CrNb_3S_6$ specimens A, B, and C. H was applied almost parallel to the direction of x-ray propagation [28] and perpendicular to the helical c axis, as seen in Fig. 2(d). Figure 2(e) shows the H dependence of M_{Cr} for the three specimens; in Fig. 2(f), the horizontal axis is converted into the effective field H_{eff} ($= H - N_{\mathrm{d}}M_{\mathrm{Cr}}$), considering the demagnetization effect of thin specimens. With the demagnetization-effect calibration, the data for specimens A and B approach those for the bulk crystals [the black solid squares in Fig. 2(f)], suggesting the appropriateness of this calibration. The critical field H_{c} in the forced-ferromagnetic state for specimen C is slightly higher than those for A and B. The helimagnetic [Fig. 1(a)], CSL [Fig. 1(b)], and forced-ferromagnetic [Fig. 1(c)] spin alignments appear for $H_{\mathrm{eff}} = 0$, $0 < H_{\mathrm{eff}} < H_{\mathrm{c}}$, and $H_{\mathrm{eff}} > H_{\mathrm{c}}$, respectively. In the following, we explain how the magnetization curves are different depending on the geometry of the

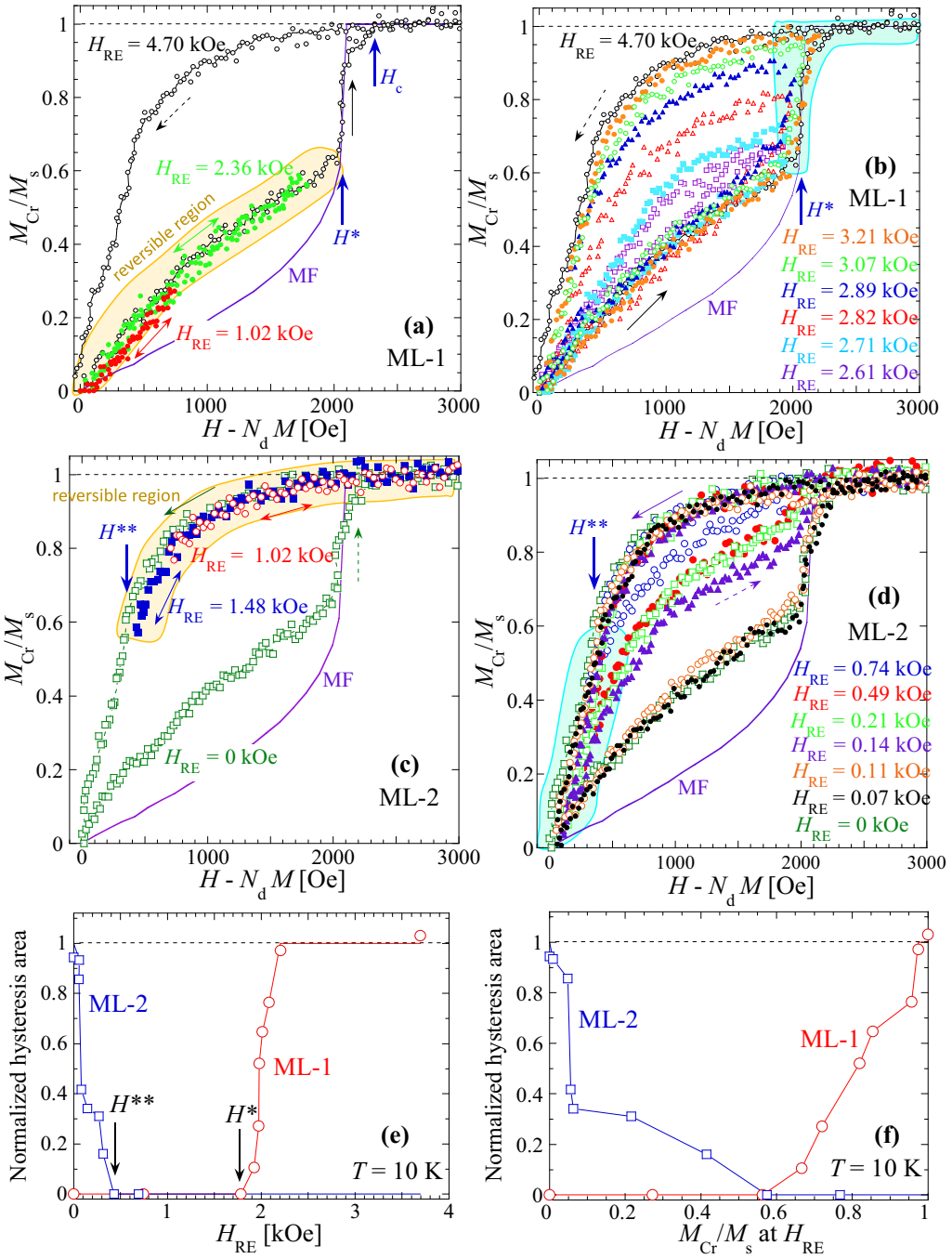

FIG. 3. Minor loop (ML) magnetization curves of specimen C of $CrNb_3S_6$ for ML-1 and ML-2. Magnetization profiles were obtained with the soft x-ray MCD measurements at $T = 10$ K. (a) and (b) ML-1 starting from zero field. (c) and (d) ML-2 starting from above H_c. For reference, the full loop and MF theory data, shown in Fig. 2(f), are also presented in (a)–(d). The original M_{Cr} vs H data corresponding to (a)–(d) are shown in Fig. S5 [27]. (e) and (f) Hysteresis areas of ML-1 and ML-2 as a function of the return field H_{RE} evaluated by the levels of (e) H_{eff} and (f) M_{Cr}/M_s. Two hysteresis thresholds, H^* and H^{**}, appear for the H-increasing and H-decreasing processes, respectively. In (a)–(d), reversible and irreversible regions are hatched with orange and light blue, respectively.

specimens; these magnetization curves provide useful insight that aids the control of the TMS number.

Specimen A [Fig. 2(a)] has high walls with thicknesses of approximately 1 μm at both edges perpendicular to and on one side along the c axis. With increasing H_{eff}, this specimen exhibits a change in the slope of M_{Cr} at approximately 1.7 kOe, followed by an almost linear dependence on H_{eff}, as shown in Fig. 2(f). This behavior arises from the decrease in the TMS number and is consistent with the MF picture [the purple curve in Fig. 2(f)] where the minimum-energy states are traced continuously [5]. At the critical field of $H_c = 2$ kOe, the saturated forced-ferromagnetic state appears. In the H-decreasing process, M_{Cr} exhibits a prominent reduction at $H_{eff} = 1.0$ kOe and subsequently returns to the original curve.

The fall of M_{Cr} corresponds to approximately half of the saturation magnetization M_s, suggesting that approximately half of the total TMSs (approximately 50 TMSs) penetrate simultaneously at this point. The behavior of a sharp jump has also been observed in the magnetoresistance measurements for a specimen with similar geometry [16].

Specimen B [Fig. 2(b)] has a geometry that is similar to that of specimen A, with its surrounding walls at one end of the c axis and both sides parallel to c axis. The large M_{Cr} jump occurs at a smaller field strength in the H-decreasing process, whereas the shape of the M_{Cr} curve resembles that of specimen A in most areas.

Specimen C [Fig. 2(c)] has a uniform thickness with no surrounding walls. Figure 2(f) shows the M_{Cr} behavior of specimen C, indicated by red solid dots. In the H-increasing process, the M_{Cr} curve appears to be temporarily saturated toward approximately 2 kOe and subsequently shows the rapid M_{Cr} growth observed in specimens A and B. An upward convex curvature is seen below approximately 2 kOe, which is distinct from the behavior observed in specimens A and B, as well as the downward convex curvature based on the MF theory [5]. The monotonic decrease of M_{Cr} without a prominent fall in the H-decreasing process is also in contrast to specimens A and B and reminiscent of that given by the Langevin function (see Fig. S3 [27]). The disappearance of the signal drop in the H-decreasing process is also found in the magnetoresistance measurements in the specimens with dimensions similar to those of specimen C (see Fig. S4 [27]). These two significant findings strongly suggest that there are unexpected magnetization profiles along which the TMS number changes between the maximum value and zero.

To identify all possible profiles for specimen C, the minor loops (MLs) of M_{Cr} were examined in various H routes, as shown in Figs. 3(a)–3(d) (see also Fig. S5 [27]). The result of the full loop shown in Figs. 3(a)–3(d) was obtained in a new run different from that for Figs. 2(e) and 2(f) to confirm the reproducibility of the characteristic behavior. The H_{eff} regions hatched with orange color in Figs. 3(a) and 3(c) exhibit reversible magnetization and demagnetization, respectively.

In the first type of ML (called ML-1), M_{Cr} is measured while increasing H from zero to the returning field H_{RE} and subsequently reducing to zero field. H_{RE} is described as the field value before calibrating for the demagnetization effect. With H_{RE} set at less than a certain field marked by H^*, no hysteresis is observed, as shown in Fig. 3(a). Once H_{RE} exceeds H^* [the H_{eff} region hatched with light blue in Fig. 3(b)], M_{Cr} does not return along the initial curve. With increasing H_{RE}, new profiles occur in the hysteresis region, as shown in Fig. 3(b).

When the MLs are taken by reducing H from above H_c and reversing the sweep direction at H_{RE} (ML-2), the onset of H_{RE} below which the hysteresis appears is also observed [the H_{eff} region hatched with light blue in Fig. 3(d)]. As shown in Figs. 3(c) and 3(d), the magnetization profile deviates from the original curve when H_{RE} decreases to below 0.4 kOe, defined as H^{**}. The area of ML obtained with H_{RE} very close to zero field [e.g., at 0.14 kOe in the H level, represented by the purple solid triangles in Fig. 3(d)] is approximately half of the area of the full hysteresis.

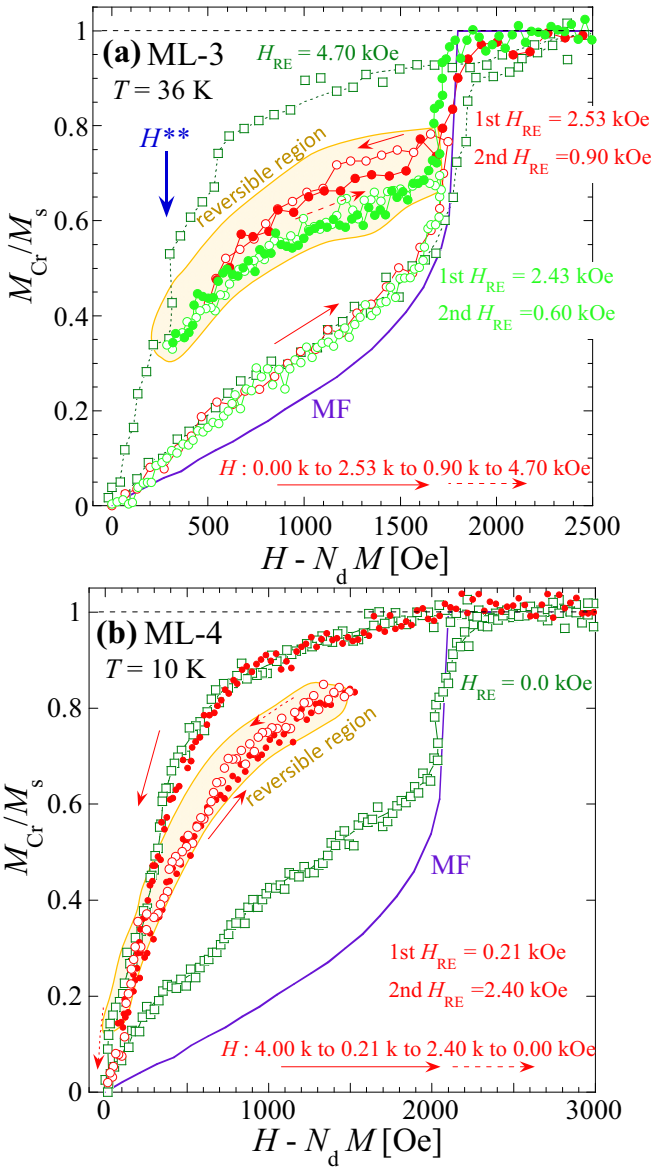

FIG. 4. Minor-loop (ML) magnetization curves of specimen C of $CrNb_3S_6$ for ML-3 and ML-4. Magnetization profiles were obtained with the soft x-ray MCD measurements. (a) ML-3 at $T = 36$ K and (b) ML-4 at $T = 10$ K. The original M_{Cr} vs H data are shown in Fig. S6 [27]. Here, the data after the field calibration are shown. The ML-3 process is $H = 0.00 \rightarrow 2.53 \rightarrow 0.90 \rightarrow 4.70$ kOe and $H = 0.00 \rightarrow 2.43 \rightarrow 0.60 \rightarrow 4.70$ kOe; the ML-4 process is $H = 4.00 \rightarrow 0.21 \rightarrow 2.40 \rightarrow 0.00$ kOe. The reversible H_{eff} regions are hatched with orange.

To identify the critical point for the appearance of the ML hysteresis, the hysteresis area obtained by integrating M_{Cr} with respect to H is plotted as a function of H_{RE} and the corresponding value of M_{Cr} at H_{RE}, as shown in Figs. 3(e) and 3(f), respectively. The figures clearly show the coincidence of M_{Cr} values at H^* for ML-1 and H^{**} for ML-2, which reveal that the ML hysteresis appears when the magnetization reaches approximately 60% of M_s in both H-increasing and H-decreasing processes. Furthermore, other types of MLs with two H_{RE} points (e.g., see ML-3 and ML-4 in Fig. 4) indicate

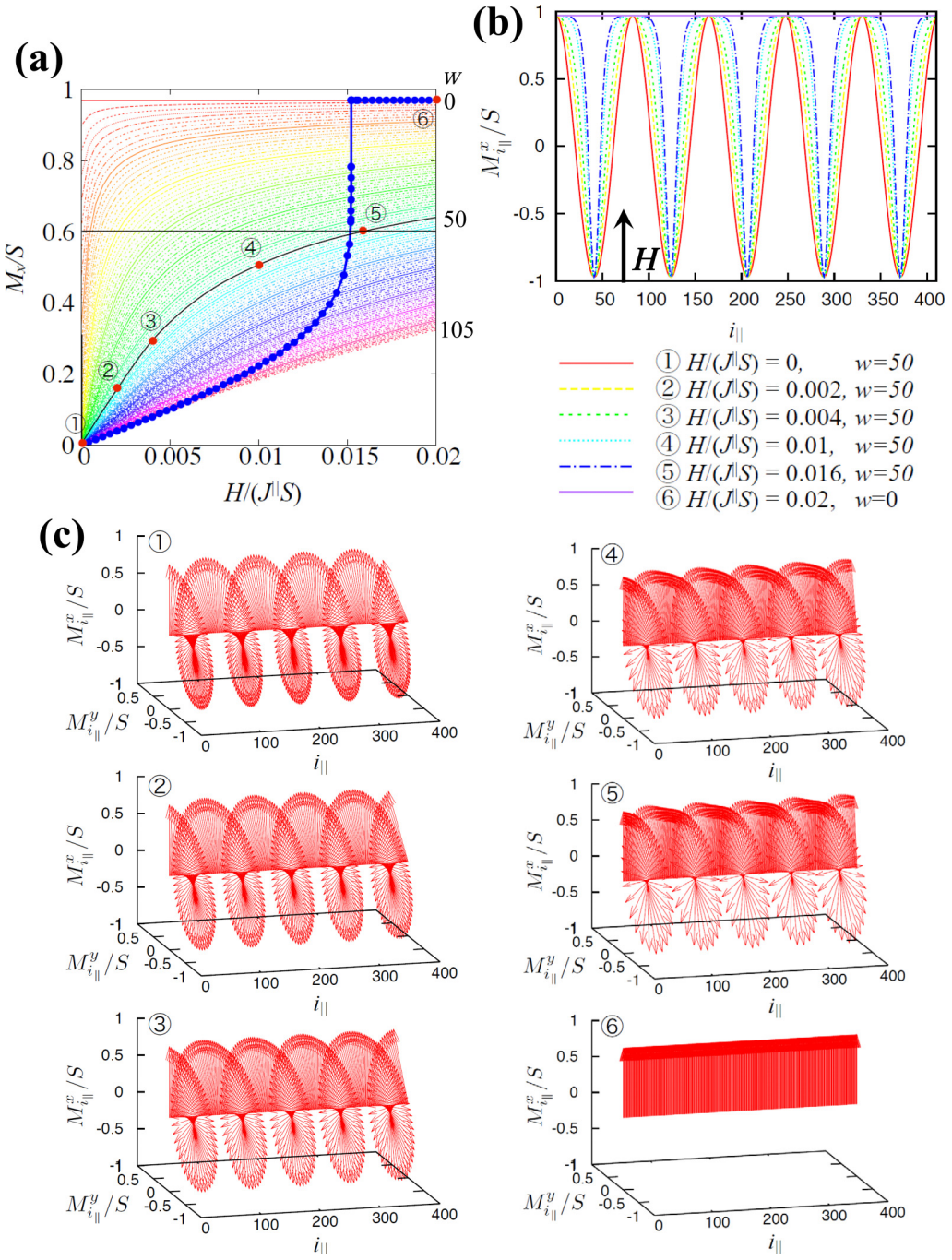

FIG. 5. (a) Theoretical calculation of the magnetization curve with fixed soliton numbers by finite-temperature three-dimensional mean-field theory under a periodic boundary condition. The soliton number w was fixed at values between 0 and 105. Points 1–5 have the same TMS number of $w = 50$, and for point 6, corresponding to the forced-ferromagnetic state, $w = 0$. (b) Spatial distributions of magnetic moments viewed from the direction perpendicular to the chiral helical axis are displayed for each point. (c) Spatial distributions for each point are displayed in three-dimensional perspectives.

that, when the H sweep direction reverses at any H value between the critical values of H^* and H^{**}, the $M_{\rm Cr}$ curve traces back to the previous profile in the hysteresis region. Thus, such robust profiles drawn within the hysteresis region may reflect the individual paths characterized by the TMS number. ML-1 and ML-3 can occur in specimens A and B, whereas ML-2 and ML-4 are characteristic of only specimen C. In order to understand these experimental findings, they are compared with theoretical calculations below.

IV. DISCUSSION

A. Three-dimensional mean-field theory

To interpret the $M_{\rm Cr}$-$H_{\rm eff}$ curves for all the specimens, we perform numerical analysis. Figure 5(a) shows a series of magnetization curves for the CSL formation with the TMS number w fixed at different values between 0 and 105. The same data are also displayed in Figs. 6(a) and 6(b) for comparison with experimental data. The calculations were obtained

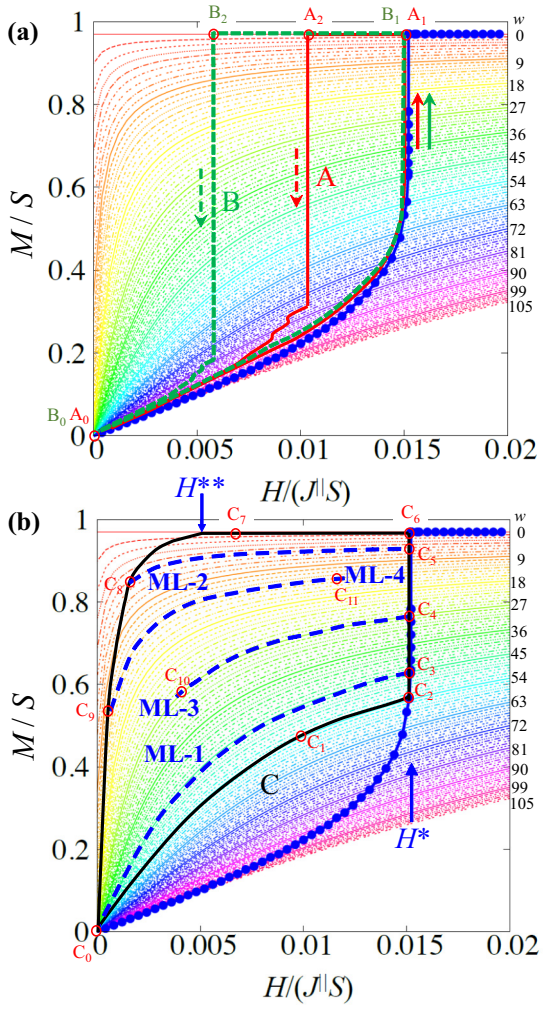

FIG. 6. Explanation of M_{Cr} for specimens A, B, and C with the help of the 3D-MF theory. In (a), guide curves and lines are shown for both specimens A ($A_0 \rightarrow A_1 \rightarrow A_2 \rightarrow A_0$) and B ($B_0 \rightarrow B_1 \rightarrow B_2 \rightarrow B_0$). The arrows in (a) indicate the directions of change in H. In (b), the full loop and four minor loops (ML-1, ML-2, ML-3, ML-4) for specimen C are indicated by solid and dashed curves, respectively. In (b), some points are labeled as C_n ($n = 0$–11), and the full and minor loops are expressed as follows: full loop, point $C_0 \rightarrow C_1 \rightarrow C_2 \rightarrow C_6 \rightarrow C_7 \rightarrow C_0$; ML-1, $C_0 \rightarrow C_1 \rightarrow C_0$ or $C_0 \rightarrow C_2 \rightarrow C_3 \rightarrow C_0$; ML-2, $C_6 \rightarrow C_7 \rightarrow C_6$ or $C_6 \rightarrow C_8 \rightarrow C_5 \rightarrow C_6$; ML-3, $C_0 \rightarrow C_2 \rightarrow C_4 \rightarrow C_{10} \rightarrow C_4 \rightarrow C_6$; and ML-4, $C_6 \rightarrow C_8 \rightarrow C_9 \rightarrow C_{11} \rightarrow C_9 \rightarrow C_0$. Both ML-1 and ML-2 have one H_{RE} point, whereas both ML-3 and ML-4 have two H_{RE} points. In both (a) and (b), the magnetization M in the vertical axis is normalized by the spin quantum number $S = 3/2$, and the magnetic field H is normalized by a multiple of the ferromagnetic exchange interaction on a plane perpendicular to the chiral helical axis $J^{||}$ and S.

by applying the finite-temperature 3D-MF theory under a periodic boundary condition [29], together with the results of the aforementioned MF theory represented by blue solid dots [5]. The maximum w is given in consideration of the diameter of the pinhole at which the MCD signals were measured. Each magnetization curve of the 3D-MF theory exhibits upward convexity similar to the Langevin function, in contrast to the downward convexity produced by the energy minimum state in the MF theory. Figures 5(b) and 5(c) present changes in M_{Cr} with a constant w (=50) by using one-dimensional and three-dimensional perspectives, respectively, demonstrating how the magnetization can change under the condition of a fixed w.

By using Fig. 5(a), we explain a series of MCD data. First, we schematically draw the lines labeled A and B based on Fig. 6(a). In the H-increasing process, successive transitions occur that connect the minimum-energy states. During the H-decreasing process, the supercooled forced-ferromagnetic state is formed, following which the magnetization jumps and a monotonic change occurs. Thus, the above behavior explains the M_{Cr} data in specimens A and B. The difference in the H onset for the large M_{Cr} jump indicates the role of the walls in specimens A and B in inducing a potential barrier for TMSs to penetrate the supercooled forced-ferromagnetic state.

Next, in Fig. 6(b), the following scenario may explain the M_{Cr} data in specimen C. At the very beginning of the H-increasing process, some portions of TMS are dissipated from the specimen because of small activation energies between the TMS states with different TMS numbers at quite a small H_{eff}. The M_{Cr} then grows along the profile with the TMS number fixed until $H_{eff} \leqslant H^*$, producing the upward convexity (corresponding to ML-1). For $H^* \leqslant H_{eff} \leqslant H_c$, the M_{Cr} rapidly changes via the successive transition between the minimum-energy states. When measuring the MLs in this region (under the condition that H_{RE} is above H^*), the hysteresis appears because the TMS number is already altered and can be maintained until some H points. In the H-decreasing process, the upward convexity of the M_{Cr} is obtained by assuming a constant TMS number. All ML types can be explained because the TMS number is fixed for $H_{eff} \leqslant H^*$ and $H^{**} \leqslant H_{eff}$.

B. Micromagnetic simulation

To confirm the conservation of the TMS number in the reversible region, we perform micromagnetic simulations using the Landau-Lifshitz-Gilbert equation in a flat, thin system modeling specimen C, which is the system landscape containing 500×20 unit cells, as schematized in Fig. 7(a).

Figure 7(b) shows the simulated MLs with H_{RE} equal to 1.0, 2.6, and 4.0 kOe. When H changes from 0 to 4.0 to 0 kOe ($H_{RE} = 4.0$ kOe), the normalized magnetization along the direction of H, M, exhibits an upward convex behavior for $H < 2.3$ kOe. Therefore, 2.3 kOe was considered to be the threshold for the H-increasing process H^*. After this threshold, M prominently increases, showing saturation at $H > H_c$ (=2.7 kOe). In the H-decreasing process, the M at saturation is maintained until approximately 0.6 kOe, which was therefore considered to be the threshold for the H-decreasing process H^{**}. Beyond this threshold, M shows an incremental decrease, eventually reverting to zero. The resultant hysteresis of M is similar to that observed for specimen C. In the case of $H_{RE} = 1.0$ kOe (labeled B), no hysteresis feature was observed. For $H_{RE} = 2.6$ kOe, a minor loop appears, and in the H-decreasing process, M tends to maintain the value at H_{RE}, exhibiting a prominent decrease at approximately 0.6 kOe (H^{**}). This behavior is consistent with the profile of ML-1 for specimen C.

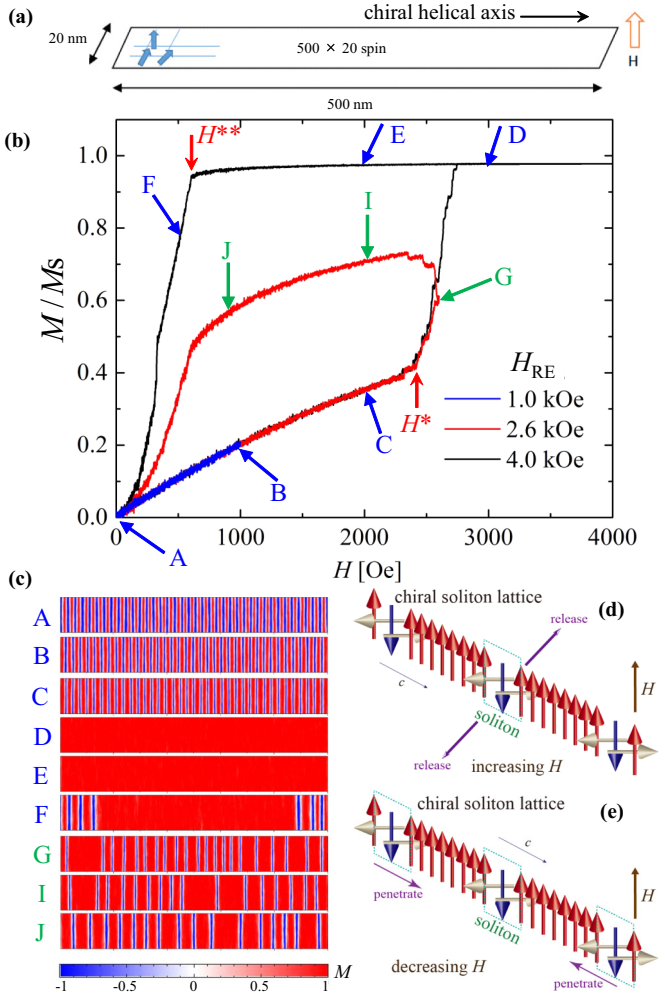

FIG. 7. Magnetization curve calculated by time evolution of the Landau-Lifshitz-Gilbert equation. (a) A microprocessed simulation was performed for the system landscape containing 500 × 20 unit cells. The magnetic field H was applied perpendicular to the chiral helical axis. (b) Dependence of the magnetization M on H for H_{RE} values of 1.0, 2.6, and 4.0 kOe. (c) The spin mapping shown at representative field points identified as A–J in (b) (A–F for $H_{RE} = 4.0$ kOe and A–C and G–J for $H_{RE} = 2.6$ kOe), where red and blue represent the positive and negative moments along H, respectively. (d) and (e) Images of the soliton's release from and insertion into the chiral soliton lattice state presented for the H-increasing and H-decreasing processes, respectively. The magnetic moments are colored according to the coloring in (c).

Snapshots of the magnetization at each H are shown in Fig. 7(c). As shown by the magnetization mapping in Fig. 7(c), the solitons assembled in A–E exhibit a regular arrangement, whereas the solitons assembled in F–J do not have a regular form. In an intuitive model, M is assumed to be $M = M_s(1 - \delta w/w_{total})$, where w_{total} and δ are the total w and the spatial distributions of the magnetic moments in the solitons, respectively. There is a difference in the spin alignment on both sides along the c axis between points A and B. Both the B and C points have the same w, although the M of point B is smaller than that of C because the territory of the nonferromagnetic configuration at B is larger than that for C. A

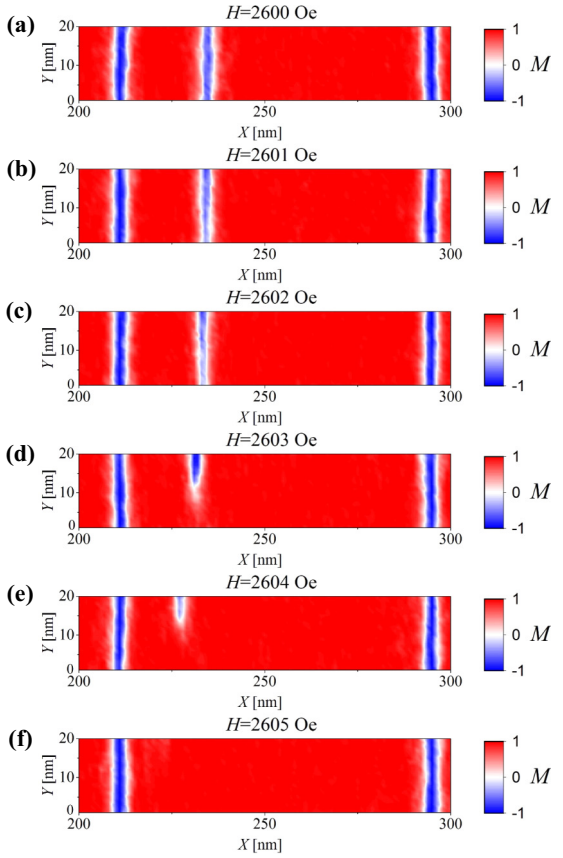

FIG. 8. Annihilation of TMSs in a flat, thin system modeling specimen C. The present system is schematized in Fig. 7(a). (a)–(f) Snapshots of the magnetization configuration (200 nm < X < 300 nm) as the number of magnetic solitons drastically changes in the hysteresis curve (as shown in Fig. 7). A series of snapshots shows how the soliton is released from the sample above H^* in the H-increasing process [from (a) to (f)].

similar phenomenon occurs between I and J. In Figs. 7(d) and 7(e), images of the soliton's release from and insertion into the chiral soliton lattice state are presented for the H-increasing and H-decreasing processes, respectively. Thus, as shown in Fig. 7(c) for points A–C, although the magnetization increases on increasing H, the soliton number is preserved below H^*. When $H > H^*$, the solitons disappear [Fig. 7(c), point G]. This soliton disappearance occurs randomly because of the magnetization fluctuation at a finite temperature. This explains the nonuniform spatial density of the soliton in Fig. 7(c) for points G–J.

Figure 8 shows the simulation of annihilation of TMSs presented in Fig. 7(d): Because we introduce the finite-temperature effect by using the random magnetic field, one soliton becomes thinner stochastically, as shown for $H =$ 2600 Oe. By increasing the magnetic field to, for example, $H = 2603$ Oe, one soliton is released from the one (upper) edge and becomes shorter at another (lower) edge, as illustrated in Fig. 7(d). Thus, the soliton is released from the direction perpendicular to the c axis.

Figure 9 shows a simulation of the creation of TMSs presented in Fig. 7(e). By decreasing H, the magnetization

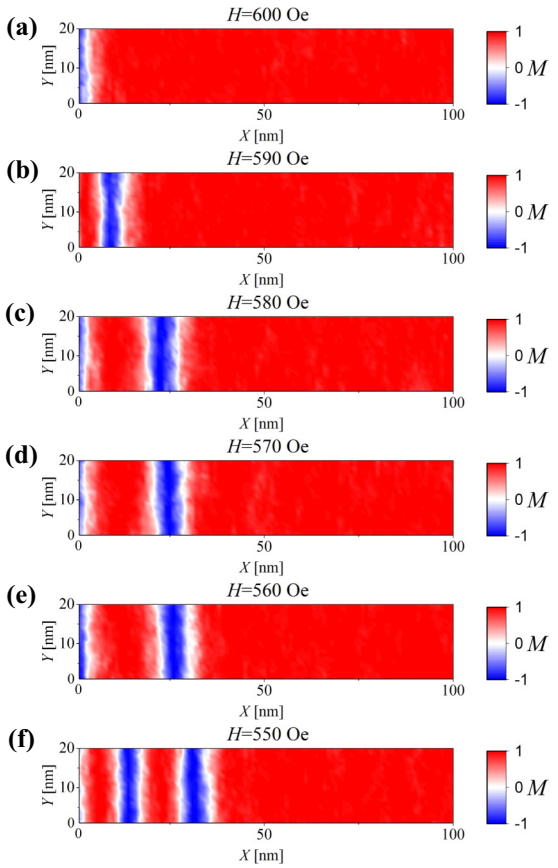

FIG. 9. Creation of TMSs in a flat, thin system modeling specimen C. The present system is schematized in Fig. 7(a). (a)–(f) show how the soliton penetrates into the sample below H^{**} in the H-decreasing process [from (a) to (f)]. The created soliton propagates to the center of the sample, while another soliton is created at the edge ($H = 580$ Oe).

can easily flip at the edge of the c axis. The created soliton propagates to the center of the sample, while another soliton is created at the edge ($H = 580$ Oe). In contrast to the soliton disappearance process, in the H-decreasing process, the soliton penetrates from the edge of the c axis. Figure 7(c), point F, also shows that the soliton is created at the edge of the specimen and propagates to the center.

Thus, the micromagnetic simulation effectively describes the hysteresis curve of specimen C obtained by MCD experiments; this hysteresis curve does not change qualitatively on considering the dipole-dipole interaction. From this soliton dynamics, the role of the high wall in specimens A and B is clear. The connecting region between the high wall and thin area easily changes the magnetization direction because of the anisotropic effect, creating solitons even in high H. Therefore, the abrupt drop in magnetization appears in specimens A and B in the H-decreasing process. A similar surface effect is discussed in relation to the magnetic-flux penetration in type-II superconductors [31–33]. From a phenomenological viewpoint, it is similar to the stripe of out-of-plane magnetization in thin ferromagnetic films in the vicinity of the reorientation phase transition [34,35]. However, the above magnetization stripe demonstrates the magnetic domain physics in the micrometer scale. In the present specimens A and B, the TEM and small-angle scattering experiments demonstrate that the magnetic solitonic texture is controllable by magnetic field [6,15,16]. The CSL formation in specimens A and B originates from a completely different mechanism of an out-of-plane magnetization stripe in thin ferromagnetic films.

V. CONCLUSION

We found that the geometry of the environment surrounding the microprocessed $CrNb_3S_6$ crystals essentially affects the TMS formation. By designing the microcrystal shapes, we demonstrated how to preserve and change the TMS number over a wide range of magnetic fields. This effect was confirmed through the experimentally observed magnetization hysteresis and was supported by MF calculations and micromagnetic simulations. The results reported here indicate that the fabricated microcrystals of the monoaxial chiral helimagnet have the functionality of a TMS valve.

ACKNOWLEDGMENTS

The authors thank K. Shibayama at KIT for support with experiments. This work was supported by Grants-in-Aid for Scientific Research, Grant No. (S) 25220803, from the Ministry of Education, Culture, Sports, Science and Technology (MEXT), Japan. This work was also supported by the Centre for Chiral Science at Hiroshima University (the MEXT program for promoting the enhancement of research universities, Japan) and the JSPS Core-to-Core Program, A. Advanced Research Networks.

[1] I. E. Dzyaloshinskii, J. Phys. Chem. Solid **4**, 241 (1958).
[2] T. Moriya, Phys. Rev. **120**, 91 (1960).
[3] N. Manton and P. Sutcliffe, *Topological Solitons* (Cambridge University Press, Cambridge, 2007).
[4] I. E. Dzyaloshinskii, Zh. Eksp. Teor. Fiz. **47**, 992 (1964) [Sov. Phys. JETP **20**, 665 (1965)].
[5] J. Kishine, K. Inoue, and Y. Yoshida, Prog. Theor. Phys. Suppl. **159**, 82 (2005).
[6] Y. Togawa, Y. Kousaka, K. Inoue, and J. Kishine, J. Phys. Soc. Jpn. **85**, 112001 (2016).
[7] S. Muhlbauer, B. Binz, F. Jonietz, C. Pfleiderer, A. Rosch, A. Neubauer, R. Georgii, and P. Boni, Science **323**, 915 (2009).
[8] T. Adams, S. Mühlbauer, C. Pfleiderer, F. Jonietz, A. Bauer, A. Neubauer, R. Georgii, P. Böni, U. Keiderling, K. Everschor *et al.*, Phys. Rev. Lett. **107**, 217206 (2011).
[9] X. Z. Yu, N. Kanazawa, Y. Onose, K. Kimoto, W. Z. Zhang, S. Ishiwata, Y. Matsui, and Y. Tokura, Nat. Mater. **10**, 106 (2011).
[10] A. O. Leonov, T. L. Monchesky, N. Romming, A. Kubetzka, A. N. Bogdanov, and R. Wiesendanger, New J. Phys. **18**, 065003 (2016).

[11] D. McGrouther, R. J. Lamb, M. Krajnak, S. McFadzean, S. McVitie, R. L. Stamps, A. O. Leonov, A. N. Bogdanov, and Y. Togawa, New J. Phys. **18**, 095004 (2016).
[12] M. N. Wilson, E. A. Karhu, A. S. Quigley, U. K. Rößler, A. B. Butenko, A. N. Bogdanov, M. D. Robertson, and T. L. Monchesky, Phys. Rev. B **86**, 144420 (2012).
[13] X. Yu, A. Kikkawa, D. Morikawa, K. Shibata, Y. Tokunaga, Y. Taguchi, and Y. Tokura, Phys. Rev. B **91**, 054411 (2015).
[14] Y. Nii, T. Nakajima, A. Kikkawa, Y. Yamasaki, K. Ohishi, J. Suzuki, Y. Taguchi, T. Arima, Y. Tokura, and Y. Iwasa, Nat. Commun. **6**, 8539 (2015).
[15] Y. Togawa, T. Koyama, K. Takayanagi, S. Mori, Y. Kousaka, J. Akimitsu, S. Nishihara, K. Inoue, A. S. Ovchinnikov, and J. Kishine, Phys. Rev. Lett. **108**, 107202 (2012).
[16] Y. Togawa, T. Koyama, Y. Nishimori, Y. Matsumoto, S. McVitie, D. McGrouther, R. L. Stamps, Y. Kousaka, J. Akimitsu, S. Nishihara *et al.*, Phys. Rev. B **92**, 220412 (2015).
[17] M. N. Wilson, E. A. Karhu, D. P. Lake, A. S. Quigley, S. Meynell, A. N. Bogdanov, H. Fritzsche, U. K. Rößler, and T. L. Monchesky, Phys. Rev. B **88**, 214420 (2013).
[18] T. Miyadai, K. Kikuchi, H. Kondo, S. Sakka, M. Arai, and Y. Ishikawa, J. Phys. Soc. Jpn. **52**, 1394 (1983).
[19] N. J. Ghimire, M. A. McGuire, D. S. Parker, B. Sipos, S. Tang, J.-Q. Yan, B. C. Sales, and D. Mandrus, Phys. Rev. B **87**, 104403 (2013).
[20] L. Wang, N. Chepiga, D.-K. Ki, L. Li, F. Li, W. Zhu, Y. Kato, O. S. Ovchinnikova, F. Mila, I. Martin *et al.*, Phys. Rev. Lett. **118**, 257203 (2017).
[21] J.-i. Yonemura, Y. Shimamoto, T. Kida, D. Yoshizawa, Y. Kousaka, S. Nishihara, F. J. T. Goncalves, J. Akimitsu, K. Inoue, M. Hagiwara, and Y. Togawa, Phys. Rev. B **96**, 184423 (2017).
[22] F. J. T. Goncalves, T. Sogo, Y. Shimamoto, Y. Kousaka, J. Akimitsu, S. Nishihara, K. Inoue, D. Yoshizawa, M. Hagiwara, M. Mito *et al.*, Phys. Rev. B **95**, 104415 (2017).
[23] J.-i. Kishine, I. G. Bostrem, A. S. Ovchinnikov, and Vl. E. Sinitsyn, Phys. Rev. B **89**, 014419 (2014).
[24] K. Tsuruta, M. Mito, Y. Kousaka, J. Akimitsu, J.-i. Kishine, Y. Togawa, H. Ohsumi, and K. Inoue, J. Phys. Soc. Jpn. **85**, 013707 (2016).
[25] K. Tsuruta, M. Mito, Y. Kousaka, J. Akimitsu, J. Kishine, Y. Togawa, and K. Inoue, J. Appl. Phys. **120**, 143901 (2016).
[26] Y. Kousaka, Y. Nakao, J. Kishine, M. Akita, K. Inoue, and J. Akimitsu, Nucl. Instrum. Methods Phys. Res. Sect. A **600**, 250 (2009).
[27] See Supplemental Material at http://link.aps.org/supplemental/10.1103/PhysRevB.97.024408 for mounting of microprocessed samples, MCD spectra, magnetoresistance, and magnetization before considering the demagnetization effect.
[28] T. Nakamura, T. Muro, F. Z. Guo, T. Matsushita, T. Wakita, T. Hirono, Y. Takeuchi, and K. Kobayashi, J. Electron. Spectrosc. Relat. Phenom **144–147**, 1035 (2005).
[29] M. Shinozaki, S. Hoshino, Y. Masaki, J. Kishine, and Y. Kato, J. Phys. Soc. Jpn. **85**, 074710 (2016).
[30] J. W. F. Brown, Phys. Rev. **130**, 1677 (1963).
[31] C. P. Bean and J. D. Livingston, Phys. Rev. Lett. **12**, 14 (1964).
[32] P.-G. de Gennes, *Superconductivity of Metals and Alloys* (Benjamin, New York, 1966).
[33] E. H. Brandt, Phys. C (Amsterdam, Neth.) **332**, 99 (2000).
[34] A. Berger and R. P. Erickson, J. Magn. Magn. Mater. **165**, 70 (1997).
[35] D. Clarke, O. A. Tretiakov, and O. Tchernyshyov, Phys. Rev. B **75**, 174433 (2007).